

Polarimetric Scene Modeling in the Thermal Infrared

M.G. Gartley, S.D. Brown, A.D. Goodenough, N.J. Sanders and J.R. Schott
Digital Imaging and Remote Sensing Laboratory
Chester F. Carlson Center for Imaging Science
Rochester Institute of Technology
54 Lomb Memorial Drive
Rochester, NY 14623-5604

ABSTRACT

Interest in polarimetric remote sensing is gaining momentum in the visible and remains strong in the microwave regions of the spectrum. However, passive polarimetric phenomenology in the 3-14 micron infrared (IR) region is complicated by the relative contributions and complementary polarization orientation of the thermally emitted and background reflected radiance. Although this modality has found success in specific missions (i.e. surface-laid landmine and tripwire detection), the dependence on time of day, scene conditions, scene geometry, collection geometry, etc. makes it difficult to easily perform empirical instrument design or tasking trade studies. This paper presents improvements to the modeling framework within the Digital Imaging and Remote Sensing Image Generation (DIRSIG) model to polarimetrically render scenes in the infrared. The DIRSIG model rigorously treats the polarimetric nature of both thermally emitted and background reflected scene radiance. The correct modeling of these two components is key to accurately predicting polarized signatures for various instrument designs and collection scenarios. The DIRSIG polarized BRDF and polarized directional emissivity models are described and compared to experimentally measured data. Results showing the sensitivity of polarimetric IR phenomenology to target and background material properties, collection geometry, and scene configuration are presented.

Keywords: Polarization, scene simulation, image simulation, BRDF, DIRSIG

1. INTRODUCTION

The optical properties of a material are generally described by the amount of light that is reflected and absorbed by the material and the amount of light emitted by the material due to blackbody radiation. The following sections will outline the theory, phenomenology and measures commonly used to characterize these effects.

1.1 Material Reflection

The incident flux reflected by a material is a combination of two generalized mechanisms. First, light is reflected by the surface of the material (e.g. the surface of a paint layer on a substrate). Second, light that is transmitted through the surface can be scattered internally by the material (e.g. the volume of the paint between the surface and the substrate) and transmitted back out the surface. Complex measurement approaches can be used to measure the magnitude of the each mechanism, however, the most common measurement approaches capture the combination of these two mechanisms. Due to the optical properties of the surface and the volume, the overall reflectance has a significant angular dependency. The directional reflectance can be characterized by the bidirectional reflectance distribution function (BRDF).¹ The BRDF captures the reflectance factor as a function of incident direction (θ_i, ϕ_i) , and reflected direction (θ_r, ϕ_r) and wavelength (λ) ,

$$\rho_{\text{BRDF}}(\theta_i, \phi_i, \theta_r, \phi_r, \lambda) = \frac{L_r(\theta_r, \phi_r, \lambda)}{E_i(\theta_i, \phi_i, \lambda)} [\text{sr}^{-1}] \quad (1)$$

where E_i is the incident irradiance and L_r is the reflected radiance. The angles θ and ϕ are the zenith (declination) and azimuth angles, respectively and the subscripts i and r indicate the incident and reflected directions, respectively. The polarization imparted on reflected light is also directionally dependent. In order to capture this dependence, polarized BRDF (pBRDF) characterizations are desired. However, there are very few materials with robust BRDF characterizations in the EO/IR region and even fewer with polarized BRDF characterizations.

Due to the number of free variables, a full BRDF measurement of a material can potentially encompass an enormous amount of data. For practical applications, parameterized BRDF models are desired for computational ease-of-use and because of the decreased storage requirements for these significantly lower dimensional representations. Most BRDFs are semi-empirical, using first-principles parameters that are empirical fit to measured data.

The integral of the BRDF over the hemisphere yields the unitless *directional hemispherical reflectance* (DHR),

$$\rho_{\text{DHR}}(\theta_i, \phi_i, \lambda) = \int_0^{2\pi} \int_0^{\pi/2} \rho_{\text{BRDF}}(\theta_i, \phi_i, \theta_r, \phi_r, \lambda) \cos(\theta_r) \sin(\theta_r) d\theta_r d\phi_r \quad (2)$$

Many materials exhibit isotropic characteristics, so the azimuthal variation can be ignored such that,

$$\rho_{\text{DHR}}(\theta_i, \lambda) = \rho_{\text{DHR}}(\theta_i, \phi_i, \lambda) \quad (3)$$

1.2 Material Absorption

Since light incident at the material surface is either reflected or transmitted into the bulk of the material, it follows that absorption must occur within the bulk of the material. Incident light that is absorbed by the material is commonly translated into thermo-mechanical energy which can result in heating of the material.

1.3 Material Emission

Any material at a temperature higher than 0 K will attempt to radiate some of that energy away. An ideal radiator is referred to as a blackbody radiator, and its radiant emittance (M) is equal to the Planck blackbody emittance which is a function of wavelength and the temperature of the material. A non-ideal radiator can only radiate a portion of this energy defined by the efficiency of a material, or the *emissivity* (ϵ). Due to a variety of surface and sub-surface geometry effects, it is generally observed that the emission is not-equal in all directions. Therefore, the radiant emittance is also a function of angle,

$$M(\theta_i, \lambda, T) = \epsilon_{\text{DE}}(\theta_i, \lambda) M_{\text{bb}}(\lambda, T) \quad (4)$$

Where $\epsilon_{\text{DE}}(\theta_i, \lambda)$ is referred to as the *directional emissivity* (DE). For materials at thermodynamic equilibrium (e.g. steady state temperature), we can assume conservation of energy and, therefore, that the absorption and emissivity are equal. Therefore, the directional emissivity can be computed from the directional hemispherical reflectance (DHR),

$$\epsilon_{\text{DE}}(\theta_i, \lambda) = 1 - \rho_{\text{DHR}}(\theta_i, \lambda) \quad (5)$$

2. MODEL DESCRIPTION

2.1 Model History

The initial development of the Digital Imaging and Remote Sensing Image Generation (DIRSIG) model was begun at Rochester Institute of Technology (RIT) in the late 1980s as a 3D simulation environment for predicting images that would be produced by thermal infrared systems. Since that time, the model has been expanded to cover the 0.35 to 20.0 micron region of the spectrum. The model is designed to produce passive broad-band, multi-spectral and hyper-spectral imagery through the integration of a suite of first-principles based radiation propagation modules. These object oriented modules address tasks ranging from bidirectional reflectance distribution function (BRDF) predictions of a surface, to time and material dependent surface temperature predictions, to the dynamic viewing geometry of scanning imaging instruments on agile platforms.² In addition to the myriad of DIRSIG specific objects that have been created, there is a suite of interface objects that leverage externally developed components (e.g. MODTRAN³ and FASCOD⁴) that are modeling workhorses for the multi- and hyper-spectral community. The software is employed internally at RIT and externally within the user community as a tool to aid in the evaluation of sensor designs and to produce imagery for algorithm testing purposes. Key components of the model and some aspects of the model's overall performance have been gauged by several validation efforts over the past decade of the model's evolution.^{5,6} The initial modification of the DIRSIG radiometry framework to support fully spectral-polarimetric radiation propagation was completed in 2002.⁷

2.2 Computational Radiometry

The DIRSIG model is a image generation tool that utilizes a complex computational radiometry sub-system to predict absolute fluxes within a 3D scene description. The model uses [1 x 4] Stokes vector and [4 x 4] Mueller matrix calculus to propagate, reflect, transmit, etc. fluxes within the simulated scene environment. When modeling signatures in the mid-wave infrared (MWIR) region (3-5 microns), the daytime illumination from the Sun is proportional to the emitted radiation from ambient (approximately 300 K) materials. Furthermore, most materials have moderate reflectances (e.g. $\rho > 0.4$) in the MWIR region and, therefore, we must consider both the reflected and the self-emission contributions to the surface leaving flux. The DIRSIG radiometry engine utilizes a single expression, governing equation across all wavelength regions such that reflected and self-emitted contributions are always included unless explicitly disabled.

2.2.1 Scene Construction

A DIRSIG scene is comprised largely of facetized models (e.g. buildings, trees, vehicles, etc.) that are created in widely available computer aided design (CAD) tools. The facetized geometry is assigned a material description which includes both thermodynamic and optical descriptions. The surface optical property model manages a flexible representation of the surface properties and allows the user to specify the BRDF, directional emissivity or both. Each material has a *radiometry solver* assigned to it. This solver object encapsulates a specific algorithm to predict the surface leaving radiance using the material optical properties. In addition to the radiometry solver, each material also has a *temperature solver* assigned to it. This solver object encapsulates a specific algorithm to predict the surface temperature using the material thermodynamic properties.

2.2.2 Surface Temperature Prediction

At this time, there is only one internal temperature solver. This solver wraps a 1D slab model named THERM that was originally developed by the DCS Corporation.⁸ This model uses 24 hours of weather to drive the radiational and convective loading of materials in the scene. The THERM model has been validated for environmentally loaded materials and demonstrated to perform well when the thermodynamic properties are well known.^{5,6} However, the THERM model does not support active loading such as a vehicle with an operating engine, a building with a heating system, etc. To model actively loaded objects, the DIRSIG model supports mechanisms to import temperatures predicted by more complex temperature prediction tools.

2.2.3 Surface Leaving Radiance Prediction

The DIRSIG model has a flexible radiometry sub-system for computing radiances for arbitrary paths within the defined scene. The primary mechanism used to predict images is *reverse ray-tracing* where rays originate from the imaging detectors and are propagated into the scene. When a ray intersects the scene geometry, the associated radiometry solver is run to compute the surface leaving radiance. DIRSIG has a handful of radiometry solvers used for opaque surfaces and the most flexible is the “generic” radiometry solver. The generic radiometry solver computes the reflected radiance by sampling the hemisphere above the target. The distribution of these samples is based on the shape and magnitude of the associated BRDF. The nominal hemispherical sampling is cosine projected and has user-defined sampling parameters (e.g. total number of samples, etc.). The incident load for those samples are determined by tracing higher generation rays which intersect other surfaces and trigger other instances of the radiometry solver. The fidelity of the sampling for higher generation bounces can be decreased using a bounce-dependent decay rate that modifies the sampling parameters. The total number of bounces that are tracked is also user controllable.

The incident loads from the sampled hemisphere are numerically integrated using the geometry specific reflectance (BRDF) and the solid angle of the sample. The incident illumination from the Sun, Moon and sky are provided by MODTRAN-P which has been integration tested with DIRSIG against Coulson’s polarized sky measurements.⁹ Since the pBRDF is accessed via surface relative incident and reflected angles, the polarization orientation of the incident illuminates must be projected into the surface relative coordinate system, and the leaving radiance must be projected into the polarization coordinates of the scene.

2.3 BRDF Modeling

The authors believe that using directional reflectance models to derive directional emissivity values has advantages over using a directional emissivity directly. In the later case, the directional hemispherical reflectance can be derived from the directional emissivity, however, the bidirectional reflectance cannot. When modeling diffuse materials, this is not an issue. However, many materials with highly polarized properties are highly specular. To correctly incorporate the directionally reflected background contributions, the full BRDF is required. Therefore, the DIRSIG modeling effort has focused on the incorporation of polarized BRDF models and numerically integrating those BRDFs to arrive at the corresponding directional emissivity.

2.3.1 Generalized BRDF Modeling

A review of the unpolarized and polarized BRDF models including those described by Torrance and Sparrow,¹⁰ Priest and Germer,¹¹ Beard and Maxwell,¹² etc. reveals a common approach. These models leverage that the Fresnel reflectance from a surface is a function of the complex index of refraction of the material ($n + ik$) and the angle of incidence. The inherent polarization built into the Fresnel reflectance functions enables these types of BRDF models to produce polarized reflectances.

The Fresnel reflectance model assumes a perfectly smooth surface and forces the reflection to have the same zenith angle as the incident ray. The generalized, micro-facet BRDF model approach treats a modeled surface as a collection of small, flat surfaces or *micro-facets* that are oriented according to a probability distribution. Each of these micro-facets can be modeled by the Fresnel reflectance function. The overall reflectance factor for a given incident and exitent geometry is a function of the probability of micro-facets oriented to produce specular reflections between the incident and exitent directions and micro-facet self-shadowing.

2.3.2 Polarized BRDF Modeling

The polarized BRDF can be generalized to include a polarized specular component and an unpolarized volume component. Although the volume component may contribute a small amount to the overall polarization of reflectance, this model treats the volume term as completely unpolarized.

$$f_{\text{pBRDF}} = f_{\text{spec}} + f_{\text{vol}} = f_{\text{polarized}} + f_{\text{unpolarized}} \quad (6)$$

The DIRSIG model includes support for several BRDF models, but the generalized, polarized BRDF model of interest in this study was implemented by James Shell and is, hereby, referred to as the “Shell Target” BRDF model.¹³ A detailed description of the Shell Target BRDF model has been reported on previously and is beyond the scope of this paper, however, a brief overview is appropriate. The specular component is modeled using the generalized, polarized micro-facet approach described previously. The micro-facet distribution is assumed to be Gaussian and the shadowing and obscuration function follows the approach presented by Beard and Maxwell and currently utilized in the Beard-Maxwell BRDF model implemented in the Non-conventional Exploitation Factors Data System (NEFDS). The unpolarized component is modeled using a compound volume scattering and diffuse scattering term.

2.3.3 Stokes Geometry Transforms

The orientation of linearly polarized light is defined with respect to the propagation direction and a reference axis that typically has some context in the real world (e.g. the “up” direction). The BRDF for a material is a function of the incident and reflected directions relative to the surface. In the case of a polarized BRDF, the polarization state (e.g. vertical linearly polarized light) is also assumed to be using the surface relative coordinate space as the reference (meaning the “up” direction is parallel to the surface normal). Once we attempt to model a surface in the context of a global coordinate system we must resolve the effects of the surface orientation within that global coordinate system. Consider vertical linearly polarized light incident on a surface that is tilted at 45 degrees about an axis in-plane with the incident light. In the context of the tilted surface, the incident light is linearly polarized but the orientation is 45 degrees rather than 0 (vertical).

To correctly reflect the radiation off of a surface arbitrarily oriented in a global coordinate system we must address two effects. First, the global incident and reflected directions must be projected into the local coordinate space so that they can be used to access the BRDF. Second, the Stokes geometry of the global incident and

reflected polarizations must be translated into and out of the the local coordinate space. The global to local vector projections required to evaluate the BRDF are common to any radiative transfer problem. However, the translation of the Stokes geometry is unique to polarized radiative transfer.

To resolve the relative vs. global Stokes geometry problem, we need to establish a rotation that will translate the polarization state into and out of a surface relative coordinate system defined by the surface normal in the global coordinate system (\hat{n}_{glob}). For a light path traveling in the direction \vec{v}_{prop} , the S (vertical) and P (horizontal) polarization orientations will be defined so that S polarization state is the global “up” direction. The P polarization state is orthogonal to both the propagation direction and S such that $\vec{v}_P \perp \vec{v}_S \perp \vec{v}_{\text{prop}}$.

The rotation for incident light (\vec{v}_i) can be determined by computing the rotation of the vertical orientation from the global coordinate system into the local coordinate system. This is accomplished by computing the angle between the surface “up” direction (defined by the surface normal, \hat{n}_{glob}) and the global “up” direction (\hat{z}_{glob}) in the plane orthogonal to the incident light. The calculation of this angle requires calculation of the S and P unit vectors of the incident light propagation direction as well as the facet normal vector projected into the S - P plane of the incident light (\vec{n}_{iSP}),

$$\hat{v}_p = \vec{v}_i \times (\hat{z}_{\text{glob}} \times \vec{v}_i) \quad (7)$$

$$\hat{v}_s = \vec{v}_i \times \hat{v}_p \quad (8)$$

$$\vec{n}_{iSP} = \vec{v}_i \times (\hat{n}_{\text{glob}} \times \vec{v}_i) \quad (9)$$

The incident rotation angle, α_i , can be computed as the inverse tangent of the ratio of the S and P components of the vector \vec{n}_{iSP} ,

$$\alpha_i = \tan^{-1} \left(\frac{\vec{n}_{iSP} \cdot \hat{v}_s}{\vec{n}_{iSP} \cdot \hat{v}_p} \right) \quad (10)$$

This angle can be used to construct a Mueller matrix that will rotate the incident Stokes vector from the global Stokes geometry into the surface relative Stokes geometry,

$$M_{\alpha_i} = \begin{bmatrix} 1 & 0 & 0 & 0 \\ 0 & \cos(2\alpha_i) & \sin(2\alpha_i) & 0 \\ 0 & -\sin(2\alpha_i) & \cos(2\alpha_i) & 0 \\ 0 & 0 & 0 & 1 \end{bmatrix} \quad (11)$$

The surface relative to global rotation angle for a similar exitent geometry (α_e) can be computed using the same approach. However, the rotation angle is opposite in sign compared to the similar incident geometry. The reflected polarized radiance (L_r) for polarized incident light is then,

$$L_r = M_{\alpha_e} \cdot (M_{\text{BRDF}} \cdot (M_{\alpha_i} \cdot E_i)) \quad (12)$$

where M_{α_e} is the local to global (exitent) Stokes rotation matrix, M_{BRDF} is the Mueller matrix from the polarized BRDF for the incident/exitenteflected geometry, M_{α_i} is the global to local (incident) Stokes rotation matrix and E_i is the incident irradiance defined in the global Stokes coordinate system. The self-emitted polarized radiance (L_e) is then,

$$L_e = M_{\alpha_e} \cdot (M_e \cdot L_{\text{bb}}) \quad (13)$$

where M_{α_e} is the local to global (exitent) Stokes rotation matrix, M_e is the Mueller matrix from the polarized directional emissivity and L_{bb} is the blackbody radiance.

3. DATA COLLECTION

3.1 Polarized Image Collection System

The collection system for all data included in this paper consisted of an long-wave infrared (LWIR) camera equipped with a single, rotatable wire grid polarizer. The LWIR camera was an EZTherm (manufactured by Electrophysics Corporation) which utilizes an uncooled Barium-Strontium-Titanate (BST) array. The camera collects 12-bit imagery at 30 frames per second and is capable of measuring blackbody temperatures between

-20C and +500C. Radiometric calibration of the camera was accomplished by imaging a blackbody cavity over a range of temperatures just prior to, or just after image collections. This calibration relates the image digital counts to aperture reaching radiances for all acquired images.

The polarizer was a 75 mm diameter, clear aperture, wire grid polarizer manufactured by Molelectron Detector, Inc. The wire grid is a fine, micro-patterned mesh of aluminum wires on a ZnSe substrate that transmits and reflects light. Wire grid polarizers are superior to the other types of polarizers due to their high contrast ratio and high transmission factors. The contrast ratio, defined as the amount of light transmitted with the appropriate polarization state to the amount of light transmitted with the incorrect polarization state, is reported by the manufacturer to be better than 400:1.

Placing the wire grid polarizer in front of the uncooled LWIR camera not only reduces the scene radiance incident on the camera aperture (due to the transmissive characteristics of the polarizer), it also reflects the thermally emitted radiance from the inside of the uncooled camera assembly (due to the reflective characteristics of the polarizer). The first problem this causes is a structured ghost image of the inside of the camera superimposed onto the scene image. The second problem this causes is a increase in the noise induced by the ghost image, which drastically increases the noise equivalent delta temperature (NEDT) of the resulting image. The camera manufacturer reports the NEDT to be 80mK under normal operation. However, incorporation of the wire grid polarizer into the optical path greatly increases the NEDT due to the two effects just described. Although the transmission of the wire grid cannot be changed, the impact of the shot-noise arising from the reflected background can be managed. The solution is to tilt the polarizer at an angle relative to the camera aperture that insures the radiance reflected from its surface comes from a uniform, cold background rather than the structured, warm background of the camera. For this experimental setup, we chose to tip the polarizer such that it reflects the night time, cloud free sky. The effective NEDT of a single frame of data taken in the manner approaches 800mK.

In order to generate the S_0 , S_1 , and S_2 Stokes images, four images were collected with the polarizer oriented at 0, 45, 90, and 135 degrees relative to the plane of incidence of the target/camera geometry. The Stokes images are derived from the intensity images as follows

$$S_0 = \frac{1}{2}(L_{SLAR}(0) + L_{SLAR}(45) + L_{SLAR}(90) + L_{SLAR}(135)) \quad (14)$$

$$S_1 = L_{SLAR}(0) - L_{SLAR}(90) \quad (15)$$

$$S_2 = L_{SLAR}(45) - L_{SLAR}(135) \quad (16)$$

The surface leaving, aperture reaching radiance (SLAR) is simply the thermally emitted and reflected background radiance terms. It is assumed that the short atmospheric path between the camera and the scene does not contribute to the overall radiance ($\tau_p \rightarrow 1$).

$$L_{SLAR}(\alpha) = \tau_p(1 - \epsilon(\alpha))L_{dw} + \tau_p\epsilon(\alpha)L_{BB} \quad (17)$$

where α is the polarizer rotation angle. The downwelled radiance L_{dw} may be measured by placing an infrared reflector in the scene possessing a surface texture and orientation similar to the targets of interest in the scene. The $L_{SLAR}(\alpha)$ image can be derived directly from the camera image after appropriately removing the skydome radiance reflected from the backside of the wire grid polarizer.

3.2 Determination of the BRDF Parameters

In addition to generating Stokes images of a scene, the same collection system was utilized to measure polarized emissivity of a variety of target and background materials. The experimental techniques and methodology used derive the parameters for the polarized BRDF model is documented elsewhere.¹⁴ The graph in Figure 1 shows the measurement derived and modeled emissivity results for a flat black painted wood target and the estimated 2-sigma uncertainty in the measurement. Due to the assumed azimuthally isotropic nature of the polarized BRDF facet distribution, there is no S_2 component for modeled polarized emissivity. The resulting polarized BRDF parameters were utilized to configure material surfaces for polarized DIRSIG image simulations.

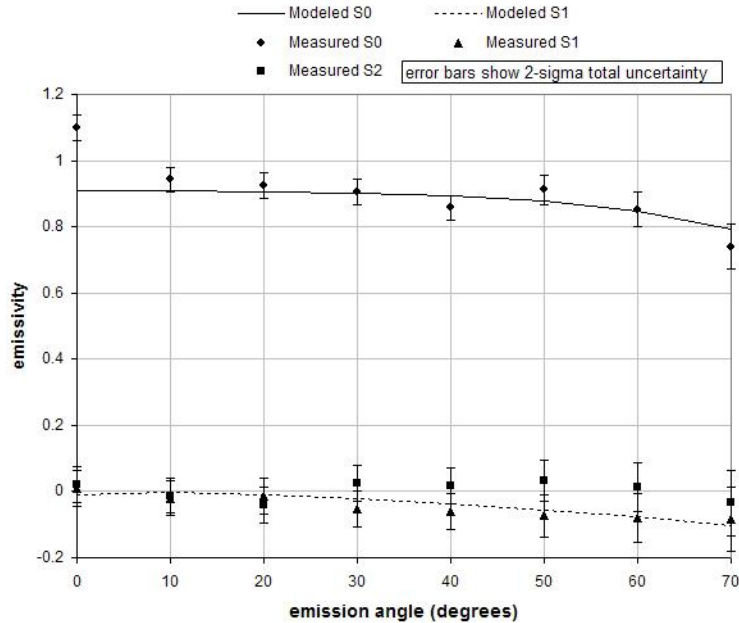


Figure 1. Plot of modeled and measured polarized emissivity for flat black painted target. The error bars show the calculated level of total measurement uncertainty at the 2-sigma level.

4. RESULTS

This section presents experimental and DIRSIG simulated results that are meant to qualitatively present expected polarimetric phenomenology in the thermal infrared. Specifically, image examples will demonstrate the effect of local surface orientation and background illumination on polarimetric signatures in the S_1 and S_2 image products. The simulated polarimetric radiance images had uniform noise added to them based on the measured noise characteristics of the actual sensor system.

4.1 Geometry Related Phenomenology

The following scenario demonstrates the effect that local surface orientation has on the polarization state of thermally emitted radiance. The first example shows a black, inflatable plastic ball on snow in front of a glossy panel imaged during the day (see Figure 2). The solar loading of the ball surface is evident in the S_0 image, i.e. the ball is much brighter than the background. In this case, the thermally emitted radiance has minimum and maximum polarization values in the S_1 image at the 12, 3, 6, and 9 o'clock positions. These minimum and maximum values correctly correspond to the vertical and horizontal orientation of the polarization expected for the self-emitted radiance. Similarly, the minimum and maximum polarization values in the S_2 bands occurs at the 1:30, 4:30, 7:30 and 10:30 positions (essentially rotated 45 degrees relative to the S_1 image).

The second dataset in this scenario is the same ball on snow in front of a glossy panel, but imaged at night under a clear, cold sky (see Figure 3). In this case, the ball temperature is roughly the same as the background temperature, leading to a polarimetric signature in the S_1 and S_2 images that is diminished relative to the previous example. The polarization of the thermally emitted radiance on the lower half of the ball is canceled out by the reflected radiance coming from the ground. In addition, the shadow of the ball in the panel surface also shows the same effect, where the polarization of the thermally emitted panel radiance is canceled by the reflection of the thermally emitted ball radiance.

4.2 Illumination Related Phenomenology

This example utilizes various target materials subjected to different types of background illumination. In the scene are nine (9) targets, including a diffuse IR reflector, a specular IR reflector, a set of various glossy painted

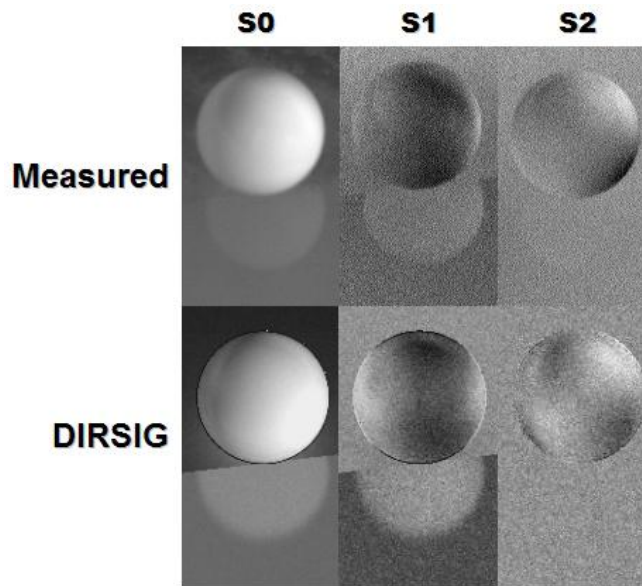


Figure 2. Measured and simulated S_0 , S_1 and S_2 images of a ball sitting on snow behind a glossy plate with a sun elevation of 18 degrees.

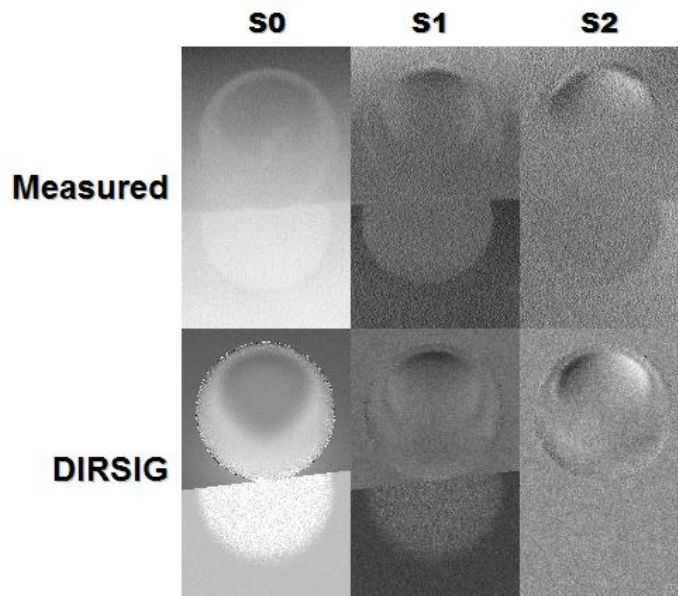


Figure 3. Measured and simulated S_0 , S_1 and S_2 images of a ball sitting on snow behind a glossy plate in front on a cold, clear night.

surfaces and a set of matte painted surfaces. In this experiment, the impact of the background illumination on scene polarimetric signatures was explored.

The first example shows the 9 targets open to the cold, clear night sky (see Figure 4). All 9 targets show polarimetric contrast in the S_1 image. Under these conditions, the thermal self-emission is expected to dominate the surface leaving radiance because the magnitude of the cold background is significantly lower. The second example shows the same target set with a small, plastic kiddie pool placed behind the targets in the specular direction (see Figure 5). The presence of the pool changes the dominantly reflected background from a cold,

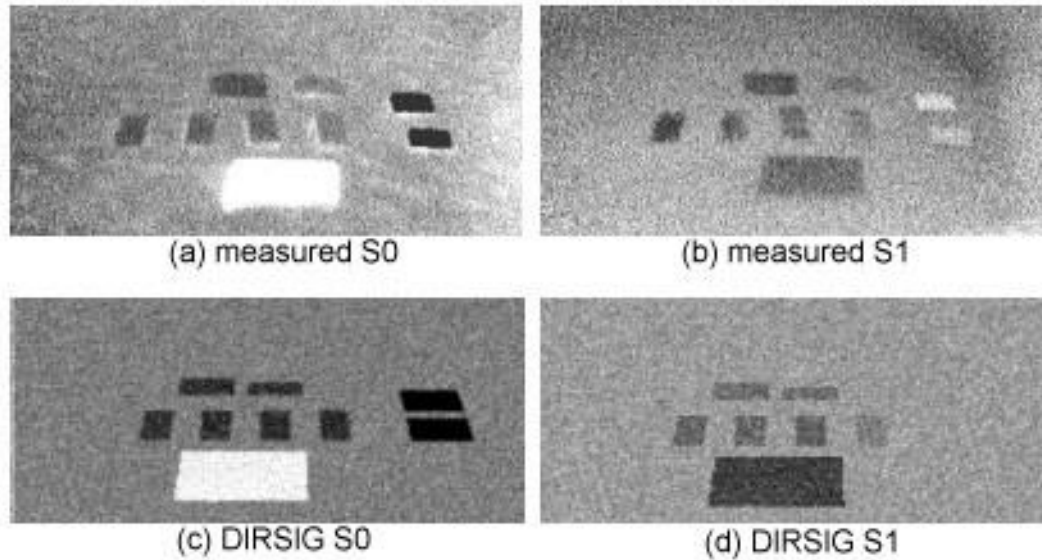


Figure 4. Measured and simulated S_0 and S_1 images of painted wood panels open to a clear night sky.

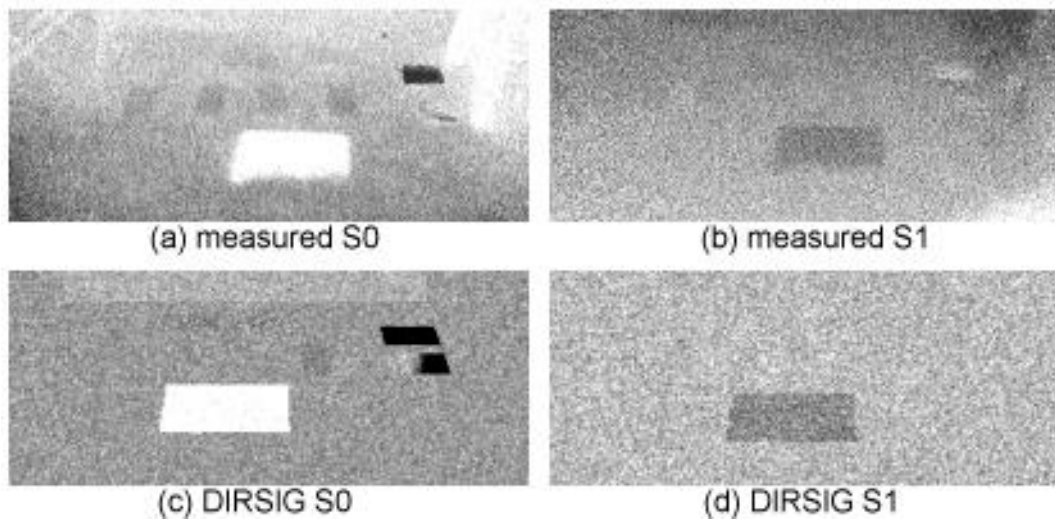


Figure 5. Measured and simulated S_0 and S_1 images of painted wood panels with a plastic pool in specular direction behind targets.

clear sky to a warm object at a approximately the temperature as the target elements. As a result, the reflected component is proportional to the self-emitted component and much of the polarization signature is canceled out by the complementary orientation of the reflected and self-emitted components.

4.3 Complex, Real-World Phenomenology

The next scenario demonstrates the polarimetric phenomenology of geometrically complex targets that are primarily open to the cold, clear sky. This candidate scene contains a VW Beetle, a sedan, and a sport utility vehicle (SUV) side by side (see Figure 6). It should be noted that the geometry models utilized in the DIRSIG simulation were only analogous to the real world objects (for example, a generic SUV model was used). In addition, only a modest effort was made to match the exact vehicle orientation and camera view geometry.

The surfaces in this scene showing the most significant polarimetric contrast in the S_1 image are the ones that

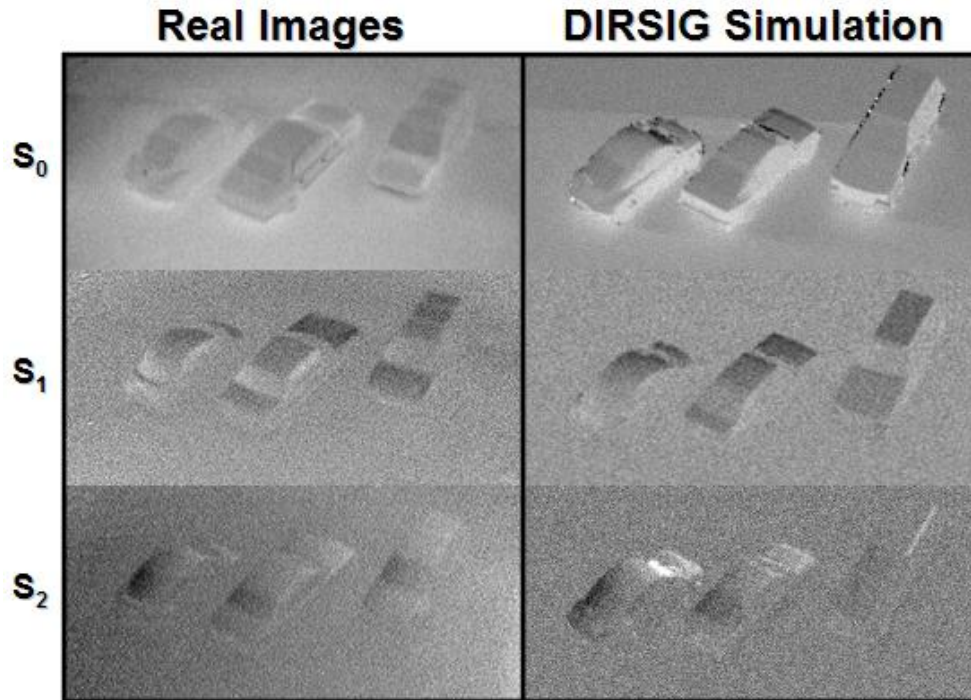


Figure 6. Measured S_0 , S_1 , and S_2 images of cars (left) and DIRSIG simulated S_0 , S_1 , and S_2 images (right)

primarily reflect the sky. Although we generally expect surfaces viewed at a grazing angle to exhibit a strong polarization signature, many of the grazing angle surfaces (such as the car sides) show almost no signature due to background reflected radiance negating the signature of the thermally emitted radiance. The surfaces that show the most significant signature in the S_2 band are ones with a relative orientation of approximately 45 degrees to the camera orientation, such as the rear windows and front right corners of the Beetle and sedan.

This example also demonstrates the strengths and weaknesses of DIRSIG's ability to effectively model scenes polarimetrically in the thermal IR. There is excellent qualitative agreement between the S_0 , S_1 and S_2 images, especially the cancellation of emission polarization signatures by background reflected radiance on the sides of the cars. However, one glaring area requiring future attention is the ability of DIRSIG to effectively model extreme grazing angles ($\theta \rightarrow 90$ degrees). The salt and pepper noise near the roof edge of the sport utility vehicle is the worst offender in this scene. The extreme grazing angle artifacts are currently believed to be due to the polarized BRDF model breaking down at extreme geometries and not the ray-tracing capability of DIRSIG.

The second real-world scenario demonstrates the polarimetric phenomenology of geometrically simple targets in a geometrically complex background. Specifically, painted panels were placed in a tree filled courtyard. Again, only modest effort has been made at this time to match the exact geometry of the trees and background structure. In the first configuration, the painted panels are placed well in front of the trees, such that the primary illumination source in the specular direction is the cold, clear sky (see Figure 7). Due to the flat nature of the scene, none of the measured imagery featured significant contrast in the S_2 image product, so they are not presented.

The second configuration places the panels directly under and in-front of a series of deciduous and coniferous trees (see Figure 8). As expected, when the background radiance from a cold source (e.g. the cold, night sky) is replaced by the much warmer radiance from the ambient trees, the vertical emissive polarization signature is negated by the horizontal reflected radiance polarization signature and the panel contrast in the S_1 product decreases.

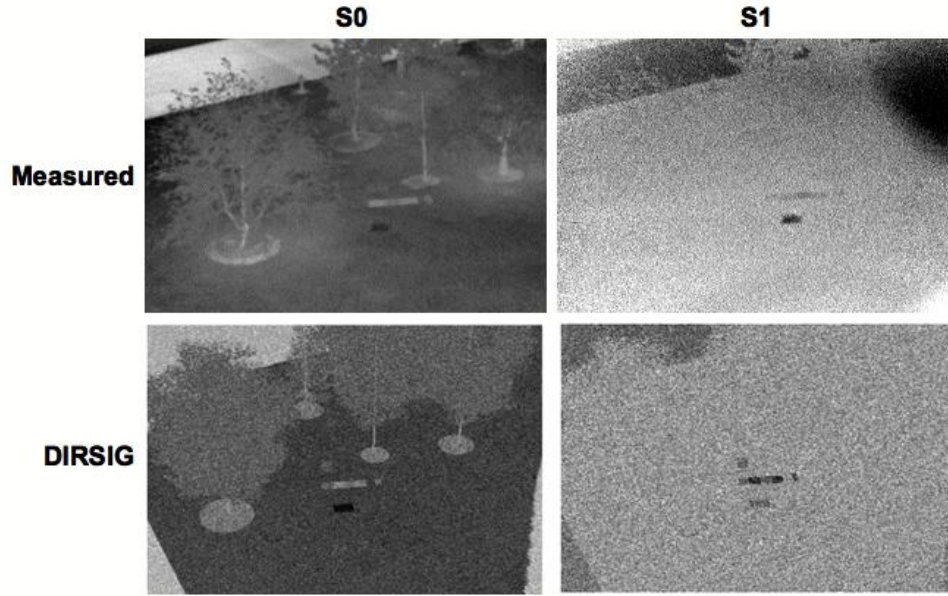


Figure 7. Measured and simulated S_0 and S_1 images of various painted surfaces placed near trees.

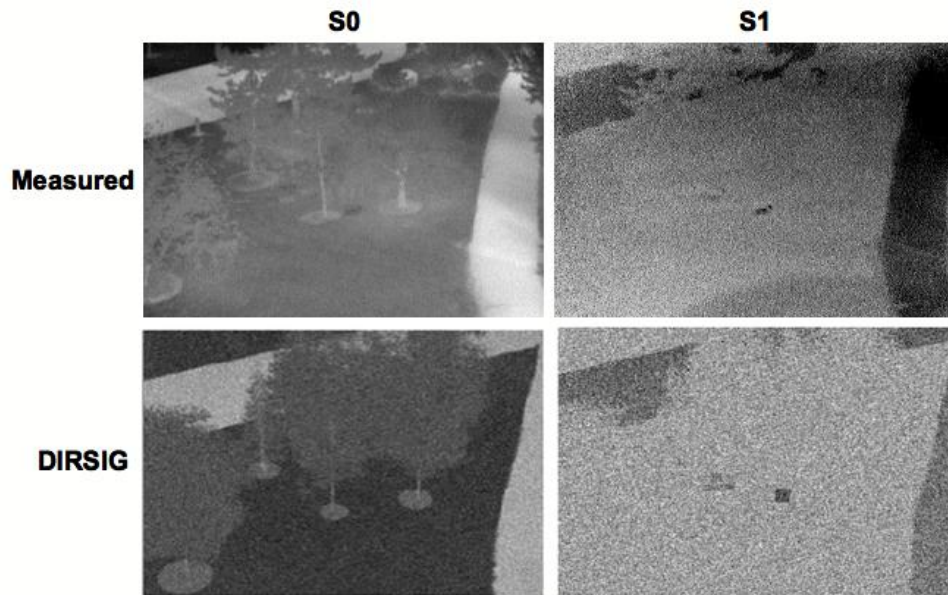


Figure 8. Measured and simulated S_0 and S_1 images of various painted surfaces placed under trees.

5. SUMMARY

The basic framework for 3D image simulation tool capability of supporting polarized imaging modalities in the thermal infrared was presented. The modeling framework leverages polarized directional reflectance models and derived polarized directional emissivity model to characterize the optical properties of materials. This approach insures that energy is conserved (hemispherical reflectance and absorption/emissivity sum to one) at all viewing geometries. The Stokes-Mueller calculus to correctly propagate reflected and self-emitted radiances from arbitrarily oriented surfaces was also described.

A modest data collection campaign was conducted to capture long-wave infrared (LWIR), polarized imagery of

various scenes. Under this effort, data collection protocols to minimize noise when using a wire grid polarizer with an uncooled LWIR camera were established. The importance of a rigorous treatment of the background reflected and self-emitted terms was demonstrated through various real-world phenomenology examples. Specifically, the relative proportion and cancellation of vertical (self-emitted) and horizontal (reflected) polarization states was shown to be dependent on background illumination conditions. The simulated data products were shown to qualitatively reproduce this observed phenomenology.

The specific BRDF model demonstrated in this paper is one of many available in the DIRSIG modeling tool. Future work may explore the use of material specific polarized BRDF models. The measured versus modeled data comparisons presented here are largely qualitative in nature, and a quantitative analysis of the model's performance is desired.

REFERENCES

1. F. Nicodemus, "Reflectance nomenclature and directional reflectance and emissivity," *Applied Optics* **9**, pp. 1474–1475, June 1970.
2. J. R. Schott, S. D. Brown, R. V. Raqueno, H. N. Gross, and G. Robinson, "An advanced synthetic image generation model and its application to multi/hyperspectral algorithm development," *Canadian Journal of Remote Sensing* **25**(2), 1999.
3. A. Berk, L. Berstein, and D. Robertson, "MODTRAN: a moderate resolution model for LOWTRAN 7," Tech. Rep. TR-89-0122, Spectral Sciences, 1989.
4. H. Smith, D. Dube, M. Gardner, S. Clough, F. Kneizys, and L. Rothman, "FASCODE- fast atmospheric signature code (spectral transmittance and radiance)," Tech. Rep. AFGL-TR-78-0081, Air Force Geophysics Laboratory, 1978.
5. J. E. Mason, J. R. Schott, and D. Rankin-Parobek, "Validation analysis of the thermal and radiometric integrity of rit's synthetic image generation model, DIRSIG," in *Proc. of SPIE, Characterization and Propagation of Sources and Backgrounds*, **2223**, pp. 474–487, 1994.
6. S. D. Brown, J. R. Schott, R. V. Raqueno, T. Kraska, and R. White, "Validation and analysis of the digital imaging and remote sensing laboratory's synthetic image generation model, DIRSIG," in *Proc. of the Seventh Annual Ground Target Modeling and Validation Conference*, 1996.
7. J. P. Meyers, J. R. Schott, and S. D. Brown, "Incorporation of polarization into the DIRSIG synthetic image generation model," in *Proc. of SPIE, Imaging Spectrometry VIII*, **4816**, pp. 132–143, 2002.
8. "AIRSIM thermal signature and prediction analysis tool, model assumptions and analytical foundations," Tech. Rep. 9090-002-001, DCS Corporation, 1990.
9. C. Devaraj, S. Brown, D. Messinger, A. Goodenough, and D. Pogorzala, "A framework for polarized radiance signature prediction for natural scenes," in *Proc. of SPIE, Algorithms and Technologies for Multispectral, Hyperspectral, and Ultraspectral Imagery XIII*, **6565**, 2007. 65650Y.
10. K. Torrance and E. Sparrow, "Theory for off-specular reflection from roughened surfaces," *Journal of the Optical Society of America* **57**, pp. 1105–1114, June 1967.
11. R. G. Priest and T. A. Germer, "Polarimetric brdf in the microfacet model: Theory and measurements," in *Proceedings of the 2000 Meeting of the Military Sensing Symposia Specialty Group on Passive Sensors*, **1**, pp. 169–181, 2000.
12. J. R. Maxwell, J. Beard, D. L. S. Weiner, and S. Ladd, "Bidirectional reflectance model validation and utilization," Tech. Rep. AFAL-TR-73-303, Environmental Research Institute of Michigan (ERIM), 1973.
13. J. R. Shell, *Polarimetric Remote Sensing in the Visible to Near Infrared*. PhD thesis, Rochester Institute of Technology, Rochester, NY, 2005.
14. M. Gartley, *Polarimetric Modeling of Remotely Sensed Scenes in the Thermal Infrared*. PhD thesis, Rochester Institute of Technology, Rochester, NY, 2007.